11th World Congress on Computational Mechanics (WCCM XI)
5th European Conference on Computational Mechanics (ECCM V)
6th European Conference on Computational Fluid Dynamics (ECFD VI)
E. Oñate, J. Oliver and A. Huerta (Eds)

RECENT PROGRESS ON A SUCTION DEPENDENT CAP MODEL FOR SOILS

PETER GAMNITZER AND GÜNTER HOFSTETTER

Institute of Basic Sciences in Engineering Science
Unit of Strength of Materials and Structural Analysis
University of Innsbruck
Technikerstrasse 13, 6020 Innsbruck, Austria
e-mail: Peter.Gamnitzer{Guenter.Hofstetter}@uibk.ac.at
web page: http://www.uibk.ac.at/bft/

Key words: Soils, Elasto-Plasticity, Smoothed Cap Model, Generalised Effective Stress, Matric Suction

Abstract. This paper provides a short report on recent progress in the development of a smooth, suction dependent cap model for soils and its application to the finite-element analysis of structures consisting of unsaturated and fully saturated soil. The governing equations for the suction dependent cap model are briefly reviewed, as well as the governing equations for the three-phase analysis of soils. Results for a fully coupled simulation of an embankment dam are used to demonstrate the capabilities of the combined approach.

1 INTRODUCTION

In general, porous geomaterials are characterised by a certain degree of permeability, allowing liquid and gaseous phases to enter and flow through the pore space of a structure matrix. The interaction between pore filling fluids and surrounding solid matrix can have a strong influence on the mechanical response of a geomaterial. Thus, for a numerical modelling approach, these interactions have to be taken into account.

The focus of this paper will be on the application of a constitutive model relating strain to generalised effective stress $\boldsymbol{\sigma}^{\text{eff}}$ and matric suction $p^c = p^a - p^w$, which equals the difference between air and water pressure, in coupled three-phase simulations. See for instance [1] for an overview on the surrounding framework. The smoothed elasto-plastic cap model [2] used here is a recent enhancement of a model which has been under constant development over several decades. Its origins date back to the well known multi-surface plasticity model [3]. More recently, this model has been extended to applications in unsaturated soils [4]. For that purpose, the model can be formulated in terms of two independent stress variables, generalised effective stress and matric suction. The yield surface is assumed to be suction dependent, the suction dependence being included via a

load-collapse yield curve, as it has also been done for instance in the Barcelona Basic Model [5]. In parallel, a further enhancement to [3] was introduced in [6] by proposing smooth transitions between the different loading surfaces, thus simplifying stress projection. This idea was included in the model [4] in [7], where a smoothing was applied not only for values of constant matric suction but was also introduced for the transition from unsaturated to fully saturated state. As described in [8], the volumetric elastic material response of the cap model for unsaturated soils was also improved such that it is now able to provide a more realistic, exponentially stiffening response.

The most recent version [2] of the model improves the above mentioned developments even further by including a number of additional features. The size of the elastic domain is now assumed to decrease in the case of plastic dilation, yielding a softening material response in the transition region between critical state and shear failure envelope. Such behaviour is also present, for instance, in the Barcelona Basic Model, and it is useful to limit plastic swelling of the material, which could occur under certain loading conditions, to a physically reasonable amount. Furthermore, in the new version, the smoothing of the surface does not affect the cohesion parameter any more as it did in [7]. An additional tensile cutoff surface was included in the smoothed cap model for unsaturated soil in [2], a new feature which proved useful especially with respect to the volumetric elastic material response, which requires a tension limit due to the assumed exponentially stiffening response used in the model. Finally, the flow rule for the shear failure envelope mode in [2] is now formulated such that the direction of the stress projection is consistent with the dependency of the yield surface on the Lode angle and the smoothness of the yield surface.

The new features simplify the model and extend the range of applicability whilst the helpful smoothness properties introduced previously are preserved. To show the new capabilities of the model, results will be presented for a coupled finite element simulation of an embankment dam.

2 A SMOOTHED CAP MODEL FOR UNSATURATED SOILS

The elastic response of the smoothed cap model for unsaturated soils is stated in rate form separately for the volumetric part (relating the first invariant of the generalised effective stress and the volumetric elastic strain ε_V^e) and the deviatoric part (relating the deviatoric stress $\boldsymbol{s}$ and the deviatoric elastic strain $\boldsymbol{e}^e$):

$$\frac{\partial}{\partial t} \ln \left(I_1^{\text{eff}} + {I_1}^{\text{eff,offset}} \right) = \frac{v}{\kappa_E} \cdot \frac{\partial}{\partial t} \varepsilon_V^e \tag{1}$$

$$\frac{\partial}{\partial t} \boldsymbol{s} = 2G \cdot \frac{\partial}{\partial t} \boldsymbol{e}^e. \tag{2}$$

Material parameters are the shear modulus G and a volumetric stiffness parameter κ_E. ${I_1}^{\text{eff,offset}}$ is a non-negative parameter which can be included to allow zero pressure stress states. The elastic strain is assumed to equal the difference between total strain and

plastic strain, i.e. $\varepsilon_V^e = \varepsilon_V - \varepsilon_V^p$ and $\boldsymbol{e}^e = \boldsymbol{e} - \boldsymbol{e}^P$, as usual. v defines the specific volume, for which under the assumption of small strains and incompressible grains, the equation

$$\frac{\partial}{\partial t} \ln v = -\frac{\partial}{\partial t} \varepsilon_V \tag{3}$$

can be obtained from the balance of mass.

The size of the elastic domain is dependent on the current value of matric suction. As it is displayed in Figure 1, the yield surface is defined by the four yield functions

$$f_{\text{Shear}} = L_\vartheta \left\| \boldsymbol{s} \right\| - \left(\alpha + F_s \left(p^c \right) + \theta I_1^{\text{eff}} \right) = 0, \tag{4}$$

$$f_{\text{Cap}} = \sqrt{\left(L_\vartheta \left\| \boldsymbol{s} \right\| \right)^2 + \left(\frac{I_1^{\text{eff}} - \kappa^{\text{eff}}}{R_{\text{Cap}}} \right)^2} - \frac{\alpha + F_s \left(p^c \right) + \theta \kappa^{\text{eff}}}{\sqrt{1 + R_{\text{Cc}}^2 \theta^2}} = 0 \ , \tag{5}$$

$$f_{\text{Cc}} = \sqrt{\left(L_\vartheta \left\| \boldsymbol{s} \right\| \right)^2 + \left(\frac{I_1^{\text{eff}} - \kappa^{\text{eff}}}{R_{\text{Cc}}} \right)^2} - \frac{\alpha + F_s \left(p^c \right) + \theta \kappa^{\text{eff}}}{\sqrt{1 + R_{\text{Cc}}^2 \theta^2}} = 0 \ , \tag{6}$$

$$f_{\text{Tc}} = \sqrt{\left(L_\vartheta \left\| \boldsymbol{s} \right\| \right)^2 + \left(\frac{I_1^{\text{eff}} - C_T \left(p^c \right)}{R_{\text{Cut}}} \right)^2} - \frac{\left(C_T \left(p^c \right) - T \right)}{R_{\text{Cut}}} = 0 \ . \tag{7}$$

They depend on three shape parameters R_{Cut}, R_{Cc}, and R_{Cap} for the elliptical yield

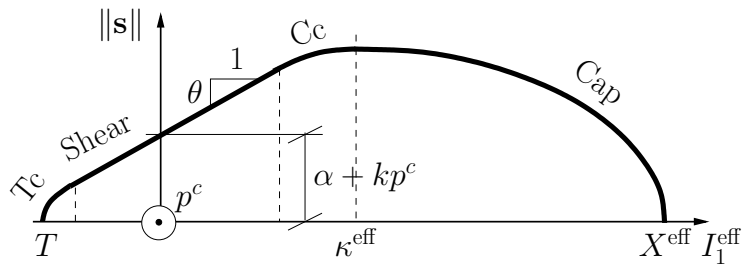

Figure 1: The yield surface of the smoothed suction dependent cap model for a fixed value of matric suction.

surfaces, the cohesion parameter α, the friction angle θ, and a tensile cutoff value T. An increase in cohesion is included via the function

$$F_s \left(p^c \right) = \begin{cases} \frac{2k}{L_{Fs}} \cdot \left(p^c \right)^2 \cdot \left(1 - \frac{p^c}{2 L_{Fs}} \right) & , \quad 0 \leq p^c < L_{Fs} \ , \\ k \cdot p^c & , \quad L_{Fs} \leq p^c . \end{cases} \tag{8}$$

The increase is controlled by the parameter k and is included with a well defined tangent at $p^c = 0$ using the smoothing parameter L_{Fs}. The centre of the elliptic tensile cutoff

surface is given by

$$C_T\left(p^c\right) = \left(\theta R_{\mathrm{Cut}}\sqrt{1+\theta^2 R_{\mathrm{Cut}}^2}+1+\theta^2 R_{\mathrm{Cut}}^2\right)T + \\ +\left(\alpha+F_s\left(p^c\right)\right)R_{\mathrm{Cut}}\left(\theta R_{\mathrm{Cut}}+\sqrt{1+\theta^2 R_{\mathrm{Cut}}^2}\right)\ , \tag{9}$$

the centre of the hardening cap and smoothed compressive corner region is given by κ^{eff}. The function L_ϑ controls the shape of the yield surface in terms of the Lode angle ϑ (see, e.g., [4, 10, 11]). In the present context, the latter is given in terms of the parameters ω, η, and the second and third invariant of $\boldsymbol{e}$, I_2^e and I_3^e:

$$L_\vartheta = \left(\frac{1-\omega\cos\left(3\vartheta\right)}{1-\omega}\right)^{-\eta}, \quad \cos\left(3\vartheta\right) = \frac{3\sqrt{3}}{2}\frac{I_3^e}{\left(I_2^e\right)^{\frac{3}{2}}}. \tag{10}$$

The shape of the yield surface is visualised in Figure 2.

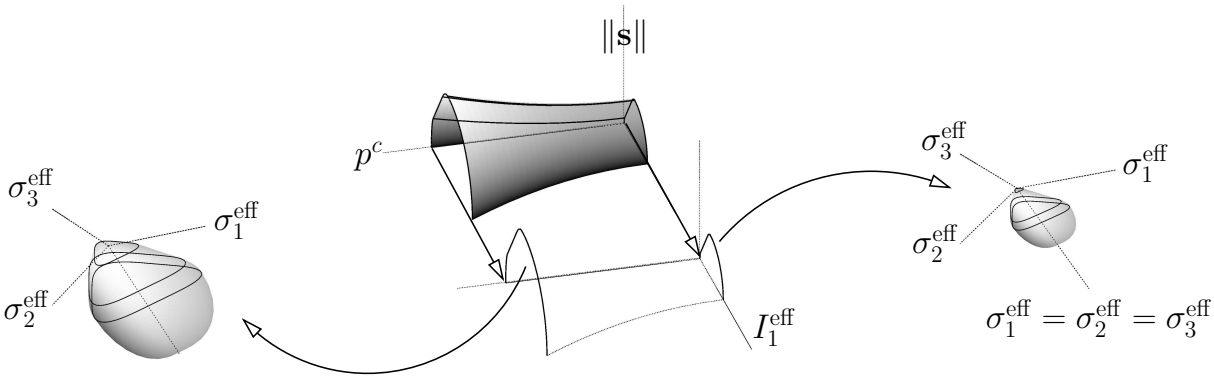

Figure 2: The yield surface of the smoothed suction dependent cap model for triaxial compression in p^c–I_1^{eff}–$\|\boldsymbol{s}\|$ space (centre). For two values of matric suction, the yield surface is also shown in principal generalised effective stress space (left and right).

X^{eff}, the intersection of the hardening cap and the hydrostatic axis, can be related to the centre of the hardening cap using

$$X^{\mathrm{eff}}\left(\kappa^{\mathrm{eff}}\right) = \kappa^{\mathrm{eff}} + R_{\mathrm{Cap}}\frac{\alpha+F_s\left(p^c\right)+\theta\kappa^{\mathrm{eff}}}{\sqrt{1+R_{\mathrm{Cc}}^2\theta^2}}\ . \tag{11}$$

It is related to its value at full saturation X^{sc} via the load collapse yield curve

$$LC^{\mathrm{net}}\left(X^{\mathrm{sc}},p^c\right) = \begin{cases} X^{\mathrm{sc}}+X_c\cdot\left(1-\exp\left(-\frac{\left(p^c\right)^2}{\sigma^2\left(p^c-p_{\max}^c\right)^2}\right)\right) & ,\ p^c < p_{\max}^c\ , \\ X^{\mathrm{sc}}+X_c & ,\ p_{\max}^c \le p^c, \end{cases} \tag{12}$$

which contains the parameters $p^c_{\max}$, σ^2, and X_c, and which is transferred to the effective stress context via a smoothed transformation

$$\begin{aligned} & I_1^{\text{eff}} \approx I_1^{\text{net}} + F_n\left(p^c\right) \quad \text{with} \\ & F_n\left(p^c\right) = \begin{cases} 3p^c \cdot \left[S_w\left(p^c\right) - 1 + \frac{2p^c}{L_{Fn}} - \frac{\left(p^c\right)^2}{L_{Fn}^2}\right] & , \quad 0 \le p^c < L_{Fn} \ , \\ 3p^c \cdot S_w\left(p^c\right) & , \quad L_{Fn} \le p^c. \end{cases} \end{aligned} \tag{13}$$

L_{Fn} is a second (numerical) smoothness parameter. (13) in combination with (12) ensures a smooth transition of the yield surface from unsaturated to saturated state. The choice of the function (12) is motivated by experimental results presented in [9]. $S_w\left(p^c\right)$, the soil-water retention curve, is approximated by the empirical relation according to [12]. Using the effective saturation S_e, it can be stated in a normalised way, and reads

$$S_e\left(p^c\right) = \frac{S_w\left(p^c\right) - S_w^r}{S_w^s - S_w^r} = \left(1 + \left(\frac{p^c}{p_b^c}\right)^{\frac{1}{1-m}}\right)^{-m} . \tag{14}$$

The rate of plastic strain is computed for each plastic mode using the non-associated flow rule

$$\frac{\partial}{\partial t}\boldsymbol{\varepsilon}^P \quad = \quad \dot{\gamma}_i \cdot \frac{\partial g_i}{\partial \boldsymbol{\sigma}^{\text{eff}}} \ . \tag{15}$$

For the plastic potentials

$$g_{\text{Shear}} \quad = \quad \|\boldsymbol{s}\| - \left(\alpha + F_s\left(p^c\right) + \theta L_\vartheta I_1^{\text{eff}}\right), \tag{16}$$

$$g_{\text{Cap}} \quad = \quad \sqrt{\|\boldsymbol{s}\|^2 + \left(\frac{I_1^{\text{eff}} - \kappa^{\text{eff}}}{R_{\text{Cap}}}\right)^2} - \frac{\alpha + F_s\left(p^c\right) + \theta\kappa^{\text{eff}}}{\sqrt{1 + R_{\text{Cc}}^2\theta^2}}, \tag{17}$$

$$g_{\text{Cc}} \quad = \quad \sqrt{\|\boldsymbol{s}\|^2 + \left(\frac{I_1^{\text{eff}} - \kappa^{\text{eff}}}{R_{\text{Cc}}}\right)^2} - \frac{\alpha + F_s\left(p^c\right) + \theta\kappa^{\text{eff}}}{\sqrt{1 + R_{\text{Cc}}^2\theta^2}}, \tag{18}$$

$$g_{\text{Tc}} \quad = \quad \sqrt{\|\boldsymbol{s}\|^2 + \left(\frac{I_1^{\text{eff}} - C_T\left(p^c\right)}{R_{\text{Cut}}}\right)^2} - \frac{\left(C_T\left(p^c\right) - T\right)}{R_{\text{Cut}}}, \tag{19}$$

the flow rule can be split in a volumetric and a deviatoric part:

$$\Delta\varepsilon_V^p = 3\Delta\gamma_i \cdot \frac{\partial g_i}{\partial I_1^{\text{eff}}} \quad , \quad \Delta\boldsymbol{e}^P = \Delta\gamma_i \cdot \frac{\partial g_i}{\partial\|\boldsymbol{s}\|} \cdot \frac{\boldsymbol{s}}{\|\boldsymbol{s}\|} \tag{20}$$

In the four modes, this expression can be evaluated using the consistency parameter in the shear failure envelope mode $\Delta\gamma_{\text{Shear}}$ and the three normalised consistency parameters

$\Delta\tilde{\gamma}_{\mathrm{Cap}}$, $\Delta\tilde{\gamma}_{\mathrm{Cc}}$, and $\Delta\tilde{\gamma}_{\mathrm{Tc}}$, in the cap, smoothed compressive corner and tensile cutoff mode as follows:

$$\Delta\varepsilon_V^p = -3\Delta\gamma_{\mathrm{Shear}} \cdot \theta L_\vartheta \quad , \quad \Delta \boldsymbol{e}^P = \Delta\gamma_{\mathrm{Shear}} \cdot \frac{\boldsymbol{s}}{\|\boldsymbol{s}\|}, \tag{21}$$

$$\Delta\varepsilon_V^p = -3\Delta\tilde{\gamma}_{\mathrm{Cap}} \cdot \frac{\kappa^{\mathrm{eff}} - I_1^{\mathrm{eff}}}{R_{\mathrm{Cap}}^2} \quad , \quad \Delta \boldsymbol{e}^P = \Delta\tilde{\gamma}_{\mathrm{Cap}} \cdot \boldsymbol{s}, \tag{22}$$

$$\Delta\varepsilon_V^p = -3\Delta\tilde{\gamma}_{\mathrm{Cc}} \cdot \frac{\kappa^{\mathrm{eff}} - I_1^{\mathrm{eff}}}{R_{\mathrm{Cc}}^2} \quad , \quad \Delta \boldsymbol{e}^P = \Delta\tilde{\gamma}_{\mathrm{Cc}} \cdot \boldsymbol{s}, \tag{23}$$

$$\Delta\varepsilon_V^p = -3\Delta\tilde{\gamma}_{\mathrm{Tc}} \cdot \frac{C_T\left(p^c\right) - I_1^{\mathrm{eff}}}{R_{\mathrm{Cut}}^2} \quad , \quad \Delta \boldsymbol{e}^P = \Delta\tilde{\gamma}_{\mathrm{Tc}} \cdot \boldsymbol{s}. \tag{24}$$

In equations (22)–(24), the Lode angle dependency of the projection direction is included implicitly in the deviatoric stress $\boldsymbol{s}$ on the yield surface, while in (22) it is included explicitly in the volumetric part of the flow rule. The formulation is designed such that the direction of the projection to the yield surface has a smooth transition between the surfaces, even if $L_\vartheta \neq 1$.

Hardening on the cap, softening on the compressive corner and shrinkage of the elastic domain in the shear envelope and tensile cutoff mode is included via the equation

$$\frac{\partial}{\partial t}\left(\varepsilon_V^p\left(\kappa^{\mathrm{sc}}, p^c\right)\right) = \lambda\left(p^c\right) \cdot \frac{\partial}{\partial t}\left(\ln\left(X^{\mathrm{net}}\left(\kappa^{\mathrm{sc}}, p^c\right)\right)\right) , \tag{25}$$

using a smoothed parameter

$$\lambda\left(p^c\right) = \lambda_0 \cdot \left(\left(1-r\right)\left(1+\beta p^c\right) e^{-\beta p^c} + r\right) . \tag{26}$$

The parameters r, β, and λ_0 are also present in the original formulation of the hardening law for the Barcelona Basic and the non-smooth cap model in [4, 5].

3 BALANCE EQUATIONS FOR THE THREE PHASE PROBLEM

In a three phase continuum, mass balance equations can be formulated for the solid, the water, and the air phase, see [1], for instance. They are stated in terms of the spatial densities in the current configuration, which are the solid density ρ^s, the water density ρ^w, and the air density ρ^a. Fluxes are governed by air velocity $\mathbf{v}^a$, water velocity $\mathbf{v}^w$, and the velocity $\mathbf{v}^s = \frac{d\mathbf{u}^s}{dt}$ of the solid phase (defined based on the solid displacement $\mathbf{u}^s$). Each of the following balance equations is stated for a control volume in the referential configuration, i.e. the time derivative has to be understood as a time derivative for a fixed

position in the undeformed configuration.

$$0 = \frac{\partial}{\partial t}\left[(1-n)\,\rho^s\right] + (\nabla \circ \mathbf{v}^s)\left[(1-n)\,\rho^s\right] \tag{27}$$

$$0 = \frac{\partial}{\partial t}\left(nS_w\rho^w\right) + (\nabla \circ \mathbf{v}^s)\left[nS_w\rho^w\right] + \nabla \circ \left(nS_w\rho^w\left(\mathbf{v}^w - \mathbf{v}^s\right)\right) \tag{28}$$

$$0 = \frac{\partial}{\partial t}\left(n\left(1-S_w\right)\rho^a\right) + (\nabla \circ \mathbf{v}^s)\left[n\left(1-S_w\right)\rho^a\right] + \\ + \nabla \circ \left(n\left(1-S_w\right)\rho^a\left(\mathbf{v}^a - \mathbf{v}^s\right)\right) \tag{29}$$

Equations (28) and (29) govern the fluid flow through the porous medium, while (27) provides a relation between pore space volume and deformation state which was already used in equation (3). The quantity n is the porosity, related to the specific volume according to $v = 1/(1-n)$.

Quasi-static equilibrium is obtained from the balance of momentum for the three phase continuum. It includes volume forces caused by gravitational acceleration $\mathbf{g}$ and reads

$$-\nabla \circ \boldsymbol{\sigma} + \left[(1-n)\,\rho^s + n\left(S_w\rho^w + (1-S_w)\rho^a\right)\right] \cdot \mathbf{g} = \mathbf{0}\ . \tag{30}$$

The sign convention used for the Cauchy stresses $\boldsymbol{\sigma}$ in this equation is pressure positive.

The fluxes in the mass balance equations are assumed to be of Darcy type, i.e. the mass-fluxes of water and gas with respect to the solid skeleton are assumed proportional to the respective phase's pressure gradient less its hydrostatic part

$$nS_w\left(\mathbf{v}^w - \mathbf{v}^s\right) = \frac{k_{w,rel}K}{\mu^w}\left(-\nabla p^w + \rho^w\mathbf{g}\right) \tag{31}$$

$$n\left(1-S_w\right)\left(\mathbf{v}^a - \mathbf{v}^s\right) = \frac{k_{a,rel}K}{\mu^a}\left(-\nabla p^a + \rho^a\mathbf{g}\right)\ . \tag{32}$$

The mass fluxes depend on the intrinsic permeability of the solid skeleton K and the dynamic viscosities μ^w, μ^a of water and air. It furthermore includes a suction dependency via the relative permeabilities $k_{w,rel}$ and $k_{a,rel}$ which accounts for the change in permeability with the degree of water saturation. Assuming a pore size distribution corresponding to the soil water retention curve (14) and following the derivations shown, e.g, in [13], the relative permeabilities are obtained as

$$k_{w,rel} = \sqrt{S_e}\left[1 - \left(1 - S_e^{\frac{1}{m}}\right)^m\right]^2 \quad \text{and} \quad k_{a,rel} = \sqrt{1-S_e}\left[1 - S_e^{\frac{1}{m}}\right]^{2m}\ . \tag{33}$$

In practice, for the applications described below, a minimum value for the relative air permeability is assumed for numerical reasons, see for instance [14].

The flux of linear momentum $\boldsymbol{\sigma}$ required in the equilibrium equation is assumed to obey the generalised effective stress concept, i.e. the generalised effective stress $\boldsymbol{\sigma}^{\text{eff}}$ acting on the solid skeleton is assumed to equal the Cauchy stress minus the weighted hydrostatic stresses of the water and air phase:

$$\boldsymbol{\sigma}^{\text{eff}} = \boldsymbol{\sigma} - p^a\left(1-S_w\right)\mathbf{1} - p^w S_w\mathbf{1}. \tag{34}$$

$\kappa_E = 0.015$	$v_0 = 1.7$	$T = 0$ MPa	$\omega = 0.6$
$G = 5.6$ MPa	$L_{Fn} = L_{Fs} = 0.3$ MPa	$R_{\text{Cut}} = 0.33$	$\eta = -0.3$
$I_1^{\text{eff,offset}} = 0.13$ MPa	$X_c = 1.4$ MPa	$R_{\text{Cap}} = 4.0$	$\lambda_0 = 0.047$
$\alpha = 23$ kPa	$\sigma^2 = 0.08$	$R_{\text{Cc}} = 0.33$	$\beta = 2\,\text{MPa}^{-1}$
$k = 0.6$	$p^c_{\max} = 1.2$ MPa	$\theta = 0.18$	$r = 0.2$
$S^s_w = 1$	$S^r_w = 0.25$	$p^c_b = 90$ kPa	$m = 0.55$

Table 1: Model parameters used in the embankment dam example.

4 USING THE MODEL IN A FINITE ELEMENT COMPUTATION

The presented model is used to examine a failure scenario for an embankment dam. It concerns the slope instability caused by water leakage through the dam. The geometry definition including the steep slope of the downstream face is adopted from a similar simulation shown in [15]. The material parameters used in the present computation are chosen such that the shape of the elastic domain in saturated state is similar to the one of the single-surface material [10] used in [15]. The choice of material properties not present in the suction-independent model [10] however is motivated by the material point tests shown in [2]. The parameters used are listed in Table 1. The problem is analysed assuming plane strain conditions. The geometry of the dam is depicted in Fig. 3. As in

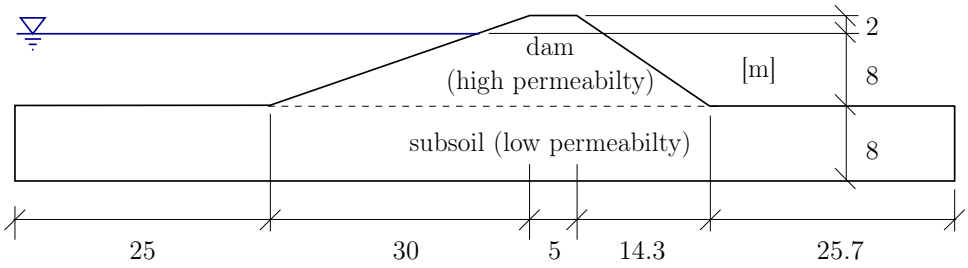

Figure 3: Geometry of the embankment dam problem.

[15], different permeabilities are assumed for the subsoil (low permeability, $\frac{\rho^w g}{\mu^w} K = 10^{-8} \frac{\text{m}}{\text{s}}$, $\frac{\rho^a g}{\mu^a} K = 10^{-9} \frac{\text{m}}{\text{s}}$) and the dam (high permeability, $\frac{\rho^w g}{\mu^w} K = 10^{-5} \frac{\text{m}}{\text{s}}$, $\frac{\rho^a g}{\mu^a} K = 10^{-6} \frac{\text{m}}{\text{s}}$). When the reservoir is filled, the water table inside the dam structure rises and finally leaking on the downstream face occurs due to the absence of a drainage.

The three-phase finite element formulation and the material model are implemented in an open source software package [16]. The structured FE-mesh used for the simulation consists of 9156 elements, characterised by quadratic serendipity shape functions for the displacements and linear shape functions for suction and air pressure with altogether

27845 nodes and 74380 unknowns. In contrast to the problem described in [15], the initial conditions for the subsoil are chosen such that it is in an unsaturated state. The initial saturation is 60%, the initial value for the hardening parameter is $\kappa_0^{\mathrm{sc}} = 0.4$ MPa.

Similar to what is reported in [15], the formation of the shear band is initiated at the toe of the dam at the downstream face (Figures 4 and 5). However, in contrast

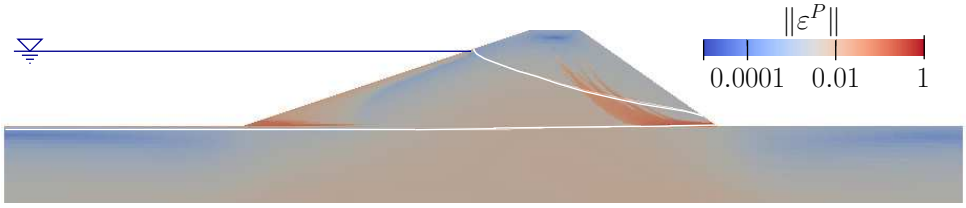

Figure 4: Shear band formation at the toe of the dam. The white line represents the phreatic surface in the dam. The norm of the plastic strains is visualised using a logarithmic scaling.

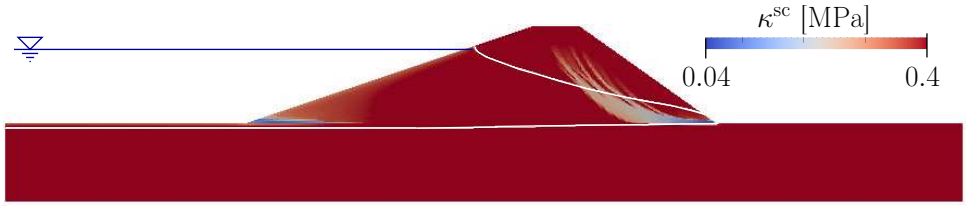

Figure 5: Shear band formation at the toe of the dam. The white line represents the phreatic surface in the dam. The visualisation of the hardening parameter κ^{sc} is based on a linear scaling.

to the results in [15], the shear band does not penetrate the subsoil, which, due to its low permeability, is still in unsaturated conditions (Figure 6) and, thus, characterised by a larger elastic domain in stress space, see Figure 2. Significant plastic strains are also

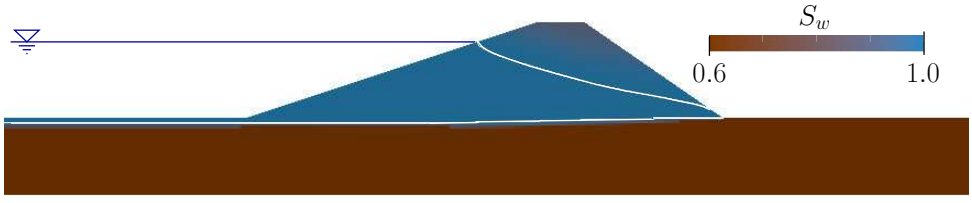

Figure 6: Distribution of water saturation.

observed on the bottom corner of the upstream face. However, an instability as for the downstream side of the dam does not occur. Eventually, the shear band extends to the other side of the dam (Figure 7). However, the magnitude of the plastic strains at this stage indicates that the results have to be treated with caution.

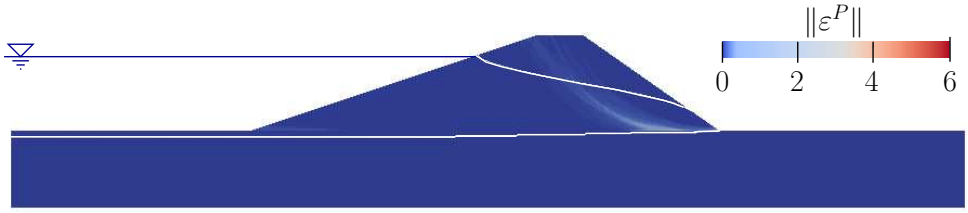

Figure 7: In the course of the computation, the shear band grows and eventually reaches the opposite face of the dam close to the crown.

5 CONCLUDING REMARKS

This paper showed the successful application of a suction dependent smoothed cap model to the coupled simulation of an earth dam. The material model was briefly reviewed, giving particular attention to the shape of the yield surface in principal effective stress space and its consequences for the appropriate definition of a smooth flow rule. Although the material model is more sophisticated than other existing models, which are often assuming linear relations between elastic strain and stress or suction independent material laws, the implementation proved to work robustly for the problem investigated.

REFERENCES

[1] Lewis, R. D. and Schrefler, B. A. The finite element method in the static and dynamic deformation and consolidation of porous media. Wiley, (1998).

[2] Gamnitzer, P. and Hofstetter, G. Efficient and robust numerical algorithms for an unsaturated soil model. In preparation.

[3] DiMaggio, F. L. and Sandler, I. S. Material model for granular soils. *J. Eng. Mech. Div.-ASCE* (1971) **97**:935–950.

[4] Kohler, R. and Hofstetter, G. A cap model for partially saturated soils. *Int. J. Numer. Anal. Meth. Geomech.* (2008) **32**:981–1004.

[5] Alonso, E. E. and Gens, A. and Josa, A. A constitutive model for partially saturated soils. Géotechnique (1990) **40**:405–430.

[6] Dolarevic, S. and Ibrahimbegovic, A. A modified three-surface elasto-plastic cap model and its numerical implementation. *Comput. Struct.* (2007) **85**:419–430.

[7] Gamnitzer, P. and Hofstetter, G. A cap model for soils featuring a smooth transition from partially to fully saturated state. *Proc. Appl. Math. Mech.* (2013) **13**:169–170.

[8] Gamnitzer, P. and Hofstetter, G. An improved cap model for partially saturated soils. *ASCE conference proceedings of the Biot conference on poromechanics V*, Vienna (2013) 569–578.

[9] Macari, E. J. and Hoyos, L. R. and Arduino, P. Constitutive modeling of unsaturated soil behavior under axisymmetric stress states using a stress/suction-controlled cubical test cell. *Int. J. Plasticity* (2003) **19**:1481–1515.

[10] Ehlers, W. A single-surface yield function for geomaterials. *Arch. Appl. Mech.* (1995) **65**:246–259.

[11] De Borst, R. and Groen, A. E. Computational strategies for standard soil plasticity models. In: Modeling in Geomechanics, edited by Zaman, M. Booker, J. and Gioda, G., John Wiley & Sons (2000) pp. 23–50.

[12] Van Genuchten, M. T. A closed-form equation for predicting the hydraulic conductivity of unsaturated soils. *Soil. Sci. Soc. Am. J.* (1980) **44**:892–898.

[13] Parker, J. C. Multiphase flow and transport in porous media. *Rev. Geophys.* (1989) **27**:311–328.

[14] Pertl, M. Grundlagen, Implementierung und Anwendung eines Drei-Phasen Modells für Böden. PhD thesis, University of Innsbruck, (2010)

[15] Ehlers, W. and Graf, T. and Ammann, M. Deformation and localization analysis of partially saturated soil. *Comput. Methods. Appl. Mech. Engrg.* (2004) **193**:2885–2910.

[16] OpenSees – the Open System for Earthquake Engineering Simulation, `http://opensees.berkeley.edu/OpenSees/home/about.php`, (2012).